Flow-small angle neutron scattering measurements of colloidal dispersion microstructure evolution through the shear thickening transition

Brent J. Maranzano[a] and Norman J. Wagner[b]
Center for Molecular and Engineering Thermodynamics, Department of Chemical Engineering, University of Delaware, Newark, Delaware 19716

(Received 23 May 2002; accepted 12 September 2002)

The shear induced microstructure for electrostatic and Brownian suspensions are compared using *in situ* small angle neutron scattering (SANS). The dispersions consist of 75 nm Stöber silica coated with 3-(trimethoxysilyl) propyl methacrylate (TPM) and have a zeta potential of -42.6 ± 4.7 mV. Neutralizing the surface charge with 0.066 *M* nitric acid yields stable hard-sphere dispersions. SANS is conducted over a range of shear rates on the charge-stabilized and Brownian suspensions to test the order–disorder transition and hydrocluster mechanisms for shear thickening, and demonstrate the influence of stabilizing forces on the shear induced microstructure evolution. Through treatment of the colloidal micromechanics, shear induced changes in the microstructure are correlated to the hydrodynamic component of the shear stress and the thermodynamic component of the normal stress, i.e., the method of ''Rheo-SANS'' is developed. The results demonstrate that hydrocluster formation accompanies the shear thickening transition. © *2002 American Institute of Physics.* [DOI: 10.1063/1.1519253]

I. INTRODUCTION

Shear thickening can occur in colloidal dispersions subjected to strong viscous flows and is accompanied by a rapid or even discontinuous increase in viscosity. It is thought that the often large and sometimes discontinuous changes in viscosity are driven by substantial changes in suspension microstructure. Two causes of reversible shear thickening have been proposed: The order–disorder transition (ODT)[1–5] and the ''hydrocluster'' mechanism.[6–11] The latter consists of a shear-induced self-organization of the colloidal microstructure under the influence of short-range hydrodynamic lubrication forces. The argument for order–disorder shear thickening supposes that at low shear rates ($\mathrm{Pe}\sim 1$) colloidal particles organize into layers or strings resulting in a lower viscosity than would be obtained for a flowing, disordered suspension. However, as the shear rate is increased, lubrication forces between neighboring particles in the highly organized, layered flow induce the particles to rotate out of alignment and destabilize the flow. Hence, the viscosity of the suspension increases due to an increase in interparticle interactions in the flowing, disordered state. Experimental evidence for an order–disorder transition accompanying shear thickening is provided by small angle light scattering by Hoffman[1–3] and some of the small angle neutron scattering measurements by Laun and co-workers[5] on charge particle suspensions. Within this framework, Hoffman,[2,12] and later Boersma and co-workers,[4] formulated physical models for shear thickening based on the balance between interparticle and shear forces to predict a critical shear rate marking the onset of shear thickening for electrostatically stabilized dispersions. However, SANS measurements on shear thickening polydisperse suspensions by Laun and co-workers[5] and hard spheres[7,13] clearly demonstrate that the ODT is unnecessary for reversible shear thickening, in agreement with simulations.[11,14]

The hydrocluster mechanism for shear thickening proposes that shear thickening is a consequence of a shear-induced self-organization of the particles into stress-bearing clusters. This self-organized microstructure is thought to be a consequence of the dominance of short-range hydrodynamic lubrication forces, whereby the flow generates transient packed clusters of particles separated from one another only by a thin solvent layer. Percolation of these hydroclusters leads to ''jamming,'' or the discontinuous, often erratic increase in shear viscosity at a critical shear stress. Evidence for the hydrodynamic basis of this phenomenon is provided by rheo-optical experiments[6,15] and stress-jump rheological measurements.[16,17] In addition, small angle neutron scattering (SANS) measurements of the shear induced microstructure support that shear thickening is accompanied by the formation of a microstructure qualitatively consistent with hydrocluster formation.[5,7,13,18–21] However, the SANS measurements demonstrating a lack of an ODT at the shear thickening transition have been criticized because measurements performed in the flow-vorticity plane may have missed transitions or melting of planes of particles oriented in the flow-vorticity plane.[12]

Finally, simulation predictions by Bossis and Brady[22] using the method of Stokesian Dynamics, and later by Boersma and co-workers,[4] and Melrose and co-workers,[10,14,23] provide computational evidence of the hydrocluster mechanism, whereas the statistical mechanical theory of Brady and co-workers[8,22,24] provides an understanding of the microstructure resulting from the singular nature of lubrication hy-

[a]Current address: PPG Industries, Pittsburgh, PA.
[b]Author to whom correspondence should be addressed. Electronic mail: wagner@che.udel.edu

drodynamics. Thus, in the hydrocluster mechanism for shear thickening, the layered or string formations are not necessary for shear thickening to occur. Bender and Wagner,[7] Melrose and Ball,[25] Mewis and co-workers,[26] and Maranzano and Wagner[27,28] have successfully developed and tested models for predicting the critical stress marking the onset of shear thickening based on the hydrocluster mechanism.

The goals of this work are two-fold: to measure and quantify the underlying three-dimensional microstructural transitions driving reversible shear thickening using *in situ* small angle neutron scattering on well characterized suspensions of weakly charge-stabilized, and near hard sphere interacting Stöber silica particles; to exploit statistical-mechanical theories linking microstructure to the mechanical stresses with the three-dimensional microstructure SANS measurements to develop a Rheo-SANS experiment. The particles chosen for study here are sufficiently small (75 ± 7.3 nm in diameter determined by transmission electron microscopy measurements) such that the first-neighbor correlation peak in the structure factor is within the wave vector range of SANS experiments. Furthermore, extensive, independent characterization of the particles and their interaction potential permits quantitative comparison with theory and simulation. The influence of particle interactions on the mechanism of shear thickening is investigated by neutralizing the weakly charged particles. This investigation probes the evolution of the suspension microstructure beginning from the equilibrium structure, through shear thinning, into the shear thickening regime to verify the mechanism responsible for shear thickening. The method employs two projections of the anisotropic scattering (i.e., tangential and radial) to resolve the three-dimensional microstructure of the dispersion. Recent work by Watanabe *et al.*[29] employed the same SANS projections with a different approach to partially reconstruct the three-dimensional microstructure. Here, these two SANS spectra under flow are quantified in terms of irreducible components of a spherical harmonic expansion. This enables reconstruction of some terms of the three-dimensional spherical harmonic expansion. The relevant components are then correlated to the hydrodynamic portion of the shear stress in the suspension to provide evidence of the increase in hydrodynamic stresses accompanying shear thickening. This constitutes a quantitative Rheo-SANS experiment, in direct analogy to the method of Rheo-Optics. These flow induced microstructure measurements can be used to critically test theory and simulation results.

II. METHODOLOGY

A detailed discussion of the particle synthesis and dispersion characterization can be found in Ref. 27, so only a brief description is presented here. The silica dispersions are prepared via the Stöber synthesis,[30–32] where seeded growth is used to obtain the desired particle size. The reaction is terminated by adding a stoichiometric quantity of a silane coupling agent, 3-(trimethoxysilyl) propyl methacrylate (TPM), which eliminates most (>98%), but not all, of the surface silanol groups.[30,33] The particles are resuspended in an index matched organic solvent; tetrahydrofurfuryl alcohol (reagent grade Aldrich, $\rho = 1.054$ g/cm^3, $n_D^{20} = 1.4512$, $\mu = 5.44$ cP), by repetitive centrifugation and suspending. The matching of the refractive indices minimizes the attractive dispersion forces, such that the resulting suspensions are weakly charge-stabilized. To study the shear thickened microstructure of hard sphere (i.e., Brownian) suspension, the remaining unreacted silanol groups are neutralized by adding aqueous nitric acid (Fisher Scientific, normality = 15.8) as suggested by Philipse.[30] These are denoted as ''charge-neutralized'' dispersions. Measurements on dilute dispersions in THFFA using a Brookhaven Zeta-PALS instrument are used to demonstrate the that a solvent molarity of 0.066 M nitric acid results in no detectable electrophoretic mobility.[33]

TABLE I. Particle characterization summary: Diameters from TEM, DLS, SANS, the rotational diffusivity from DLS, density from drying and solution densitometry, ζ-potential from electrophoretic mobility, the inverse Debye length times particle size calculated at $\phi = 0.5$.

	HS75
d_{TEM} (nm)	75 ± 7.3
d_{DLS} (nm)	88.8 ± 0.8
d_{SANS} (nm)	71.0 ± 7.0
l_{major}/l_{minor}	1.07 ± 0.06
Θ_o (s^{-1})	-100.5 ± 1.0
ρ_{SiO_2} (g/cm^3)	1.70 ± 0.01
$\rho_{particle}$ (g/cm^3)	1.45 ± 0.02
ζ (mV)	-42.6 ± 4.7
$\kappa a(\phi = 0.5)$	13.2 ± 1.3

Characterization of the dispersions is performed through a variety of experimental techniques. The particle size distribution (PSD) is determined and verified through transmission electron microscopy (TEM), dynamic light scattering (DLS), and small angle neutron scattering (SANS) measurements. DLS measurements at varying scattering angle confirm the TEM results, showing the particles to be spherical. The particle density is measured from solution densitometry and dilution viscometry experiments. Solution densitometry measures the SiO_2 density, whereas dilution viscometry estimates the density based on the hydrodynamic size of the particles. Volume fractions are calculated from drying experiments, where the densities from solution densitometry are used to convert the weight fractions to volume fractions. Further details of the particle characterization are discussed elsewhere.[27,28] These results are summarized in Table I.

In situ small angle neutron scattering measurements are performed at equilibrium, and within the shear thinning and shear thickening regimes on both the unneutralized and neutralized dispersions. The scattering data is obtained at the National Institute of Standards and Technology (NIST) in Gaithersburg, MD on a 30 m SANS instrument using thermal neutrons with a 6 Å wavelength and 14.7% half-width triangular dispersity at a sample to detector distance of 12 m, using 1 mm sandwich cells and a couette cell (10 cm DIN and 0.5 mm gap) attached to a stepper motor for static and flow measurements, respectively. Figure 1 shows the scattering geometry for both on-axis (radial) and off-axis (tangential) scattering configurations. During tangential measurements a 1.0 mm slit is used to culminate the beam through

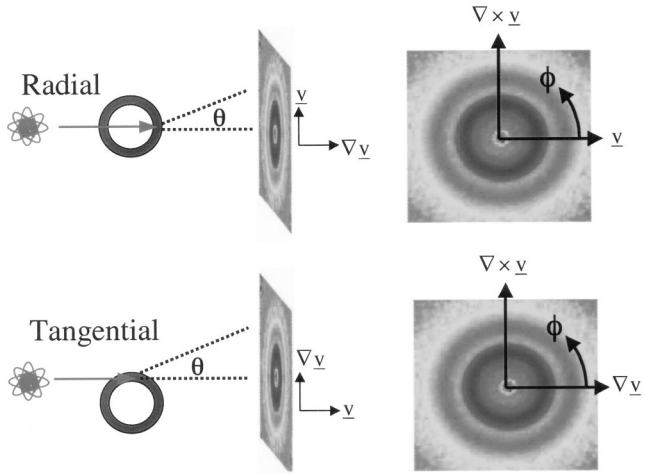

FIG. 1. Geometry of SANS scattering experiment. Note that because of the very small scattering angle ($\theta \approx 1.4°$), $\mathbf{q}_{\nabla \mathbf{v}} \approx 0$ for radial and $\mathbf{q}_{\nabla \mathbf{v}} \approx 0$ for tangential scattering.

the gap in the couette cell. The measured intensities are reduced and put on an absolute scale following standard procedures. Since the couette cell is not equipped with a torque transducer, rheological measurements are conducted in advance on a Bohlin controlled stress rheometer. The rheometer has a torque range of 0.001 to 10 mNm with a torque resolution of 0.0002 mNm and an angular deflection resolution of 1.6 μrad. The data reported here are produced with: 20 mm–4°, and 20 mm–1° cone and plates. The viscosity is measured during stress sweeps from 0.5 to 4700 Pa then returning to 0.5 Pa at 20 logarithmically spaced points. The sample is given 10 s to reach steady state at each applied shear stress followed by averaging the viscostly for 20 s.

The changes in the microstructure are qualitatively illustrated in a series of 2-D surface plots, in addition to a more quantitative assessment by circularly integrating the 2-D data weighted by trigonometric functions. The integral is evaluated numerically as a Riemann sum over the detector pixels,

$$\Delta I(q) = \frac{1}{2\pi} \int_0^{2\pi} (I(q,\theta;\dot{\gamma}) - I_{\mathrm{eq}}(q;\dot{\gamma}=0)) \cos(n\theta) d\theta;$$

$$n = 0,1,2,\ldots . \tag{1}$$

The integration of the SANS data over the azimuthal angle weighted by harmonics of the cosine provides a method to detect anisotropy and determine any special symmetry in the scattering, such as the six-fold symmetry expected for ordered latices. This is also motivated by the ability to quantitatively compare experiment with theoretical predictions of the microstructure.[34,35]

Deformations in the dispersion microstructure can be quantified with an expansion in spherical harmonics, as illustrated previously.[36] The irreducible tensor components have scalar coefficients containing the dependence of the microstructure and scattering on wave vector (q) that are denoted as $[B^{+}_{(l,m)}(q)]$. These coefficients are functions of the shear rate, which is suppressed in the notation for clarity. Here, l, m refer to the indices of the spherical harmonics.

$$\begin{aligned} S(\mathbf{q}) - 1 &= \hat{h}(\mathbf{q}) \\ &= 2B^{+}_{0,0}(q) Y_{0,0} + 2B^{+}_{2,0} Y_{2,0} + B^{+}_{2,1}(Y_{2,-1} - Y_{2,1}) \\ &\quad + B^{+}_{2,2}(q)(Y_{2,2} + Y_{2,-2}) + \ldots \ (l > 2, -L \leqslant m \leqslant l). \end{aligned} \tag{2}$$

The microstructure expansion has been quantitatively related to the hydrodynamic and thermodynamic stresses, which is the basis of Rheo-optics as well as Rheo-SANS. Note that in a colloidal dispersion, the hydrodynamic stresses arise from solvent mediated coupling that is purely fluid mechanical in origin, whereas the excluded volume and colloidal interactions (i.e., DLVO forces) arise from steric and other forces electromagnetic in nature. This distinction is important as the forces scale differently with suspension properties and the applied flow. Distinguishing between the hydrodynamic and thermodynamic contributions to the shear stresses is central to resolving which of the forces is driving the shear thickening transition. The component of the shear stress arising from hydrodynamic interactions can be calculated from the spectroscopically measured microstructure using Eq. (3):[36,37]

$$\begin{aligned} \tau_{\mathrm{hydro}}(\dot{\gamma})/2\dot{\gamma}\mu &= 1 + \frac{5}{2}\phi(1+\phi) + 2.7\phi^2 + \frac{5}{2}\phi\sqrt{\pi} \\ &\quad \times \int \Bigg[B^{+}_{0,0}(q;\dot{\gamma}) \left(2\alpha(q) + \frac{4}{15}\xi_0(q) \right) \\ &\quad + B^{+}_{2,0}(q;\dot{\gamma}) \left(\frac{2}{3\sqrt{5}}\beta(q) - \frac{4}{15}\sqrt{\frac{2}{7}}\xi_2(q) \right) \\ &\quad + B^{+}_{2,2}(q;\dot{\gamma}) \left(\frac{2\sqrt{2}}{105}\xi_2(q) + \sqrt{\frac{2}{15}}\beta(q) \right) \\ &\quad + \ldots \Bigg] q^2 \, dq. \end{aligned} \tag{3}$$

In the above equation τ_{hydro} is the hydrodynamic component of the shear stress, $\dot{\gamma}$ is the shear rate, μ is the solvent viscosity. The functions $\alpha(q)$, $\beta(q)$, $\xi_o(q)$, and $\xi_2(q)$ are hydrodynamic functions[36] that are not dependent on the deformation rate, but are only known for the limit of pairwise additive interactions. However, calculations show them to be of short range, weighting the microstructure most significantly for $q < q_{\max}$, with $q_{\max}$ the location of the first peak in S_{eq}. Furthermore, the hydrodynamic weighting functions emphasize changes in the $l=2$ components over the $l=0$ components of the expansion. Consequently, we *correlate* the change in the hydrodynamic stress to the microstructure as

$$\tau_{\mathrm{hydro}}(\dot{\gamma}) \approx C 2\dot{\gamma}\mu \int_{\mathrm{peak}} (B^{+}_{2,0}(q;\dot{\gamma}) + B^{+}_{2,2}(q;\dot{\gamma})) q^2 \, dq, \tag{4}$$

where the proportionality constant C would be termed the Stress-SANS coefficient in analogy to rheo-optics. This coefficient includes hydrodynamic coefficients that weight the integrals, as well as prefactors that include the volume frac-

tion. Based on calculations valid for hard-spheres, we estimate this coefficient to be of the order of magnitude of 10^{-2}. In the above, the harmonics coefficients, $B^+_{0,0}(q;\dot\gamma)$, $B^+_{2,0}(q;\dot\gamma)$ and $B^+_{2,2}(q;\dot\gamma)$, are calculated from the following equations, which are derived in the Appendix:

$$B^+_{0,0}(q;\dot\gamma)=\frac{\sqrt{\pi}}{3}S_{\rm eq}(q)\times(2W_{0,\rm radial}++W_{0,\rm tangential}+2W_{2,\rm tangential})-1, \tag{5}$$

$$B^+_{2,0}(q;\dot\gamma)=\frac{1}{2}\sqrt{\frac{4\pi}{5}}S_{\rm eq}(q)\times\left(\frac{-2}{3}W_{0,\rm radial}+\frac{2}{3}W_{0,\rm tangential}+\frac{4}{3}W_{2,\rm tangential}\right), \tag{6}$$

$$B^+_{2,2}(q;\dot\gamma)=2\sqrt{\frac{8\pi}{15}}S_{\rm eq}(q)W_{2,\rm radial}. \tag{7}$$

In Eqs. (5–7), $B^+_{(l,m)}(q;\dot\gamma)$ are the structure factor components obtained under shear, $S_{\rm eq}(q;\dot\gamma=0)$ is the equilibrium structure factor, and the W's are the integrals of the ratio of the nonequilibrium to the equilibrium scattering intensities, weighted by $\cos(n\phi)$, and integrated over the azimuthal angle as

$$W_n=\frac{1}{2\pi}\int_0^{2\pi}\cos(n\phi)\left(\frac{I(q,\phi;\dot\gamma)}{I_{\rm eq}(q;\dot\gamma=0)}\right)d\phi. \tag{8}$$

$W_{\rm radial}$ and $W_{\rm tangential}$ correspond to weighted patterns taken from radial and tangential scattering, respectively (Fig. 1).

Note that we use the measured equilibrium structure factor $[S_{\rm eq}(q,\phi)=I_{\rm eq}(q,\phi)/\phi/I_{\rm eq}(q,\phi_{\rm dilute})/\phi_{\rm dilute}]$ in the above equations. Due to the paucidispersity of our dispersions, the chromatic dispersion in neutron wavelength, and the detector and instrument resolutions this measured $S_{\rm eq}$ will not be precisely equal to the actual structure factor (i.e., the ''thermodynamic'' structure factor).[38] However, optimization of the experimental configuration and the colloidal dispersion have been made to minimize these ''smearing'' effects. Thus, although these stress-structure relations are valid for monodisperse suspensions and for desmeared scattering spectra, we neglect the influence of paucidispersity and instrument smearing as they are relatively minor effects for our measurements and we are correlating changes in microstructure with changes in stress.

Stokesian dynamic simulations by Brady and co-workers[39] and solutions of microstructural evolution equations[40,41] have also made predictions for the component contributions to the normal stress differences for hard sphere suspensions through the shear thickening transition. To determine the evolution of the normal stress differences, we use the following equations to semi-quantitatively predict the the first and second normal stress differences arising from *thermodynamic* interactions from the measured changes the microstructure (see Ref. 36):

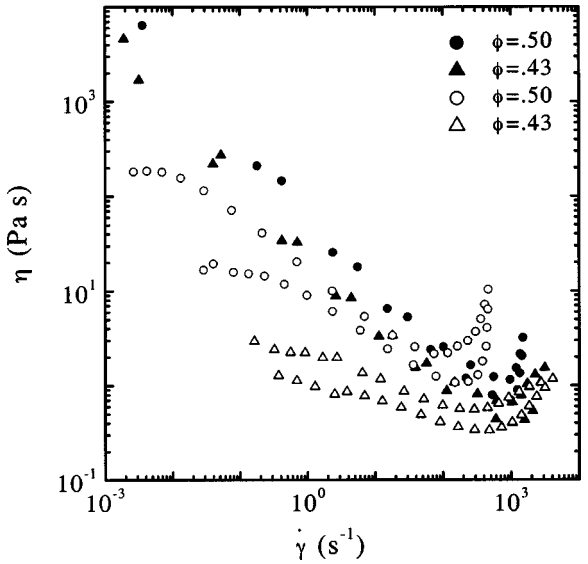

FIG. 2. Viscosities plotted against applied shear rate for the unneutralized (filled symbols) and neutralized (open symbols) dispersions at two particle concentrations ($\phi=0.5$ and $\phi=0.43$). Each viscosity measurement consists of data recorded during ascending shear stress (upper curve) and descending shear stress (lower curve).

$$\Psi_1\propto\int(B^+_{2,2}(q;\dot\gamma)-\sqrt{6}B^+_{2,0}(q,\dot\gamma))q^2\,dq,$$

$$\Psi_2\propto\int(B^+_{2,2}(q;\dot\gamma)+\sqrt{6}B^+_{2,0}(q,\dot\gamma))q^2\,dq. \tag{9}$$

Here, Ψ_i are the normal stress difference coefficients and the proportionality constant will not be the same as for the shear stresses, as these components are due to the thermodynamic and not hydrodynamic contributions. The reader is referred to the original publication for a detailed explanation and derivation of the equations.[36]

Finally, we note that the two SANS projections studied here, because of the approximation of small angle scattering, do not enable reconstruction of the important microstructure component $B^+_{2,1}(q;\dot\gamma)$, which is linked to the direct, interparticle contribution to the shear stress. Measurements of this component are possible by flow-small angle light scattering, as shown previously.[34]

III. RESULTS

Figure 2 compares the reversible shear thickening of the unneutralized and charge-neutralized dispersions at two particle concentrations ($\phi=0.5$ and $\phi=0.43$). Upon charge-neutralization the low-shear rheology changes qualitatively and a Newtonian low-shear plateau becomes evident. This is a consequence of decreasing the effective particle concentration due to the removal of the weak electrostatic interactions. Furthermore, the concentrated dispersions exhibit some hysteresis, where the viscosity is higher for data recorded during the ascension of the applied shear stress than for that recorded during the descension of shear stress. This is particularly evident in the neutralized dispersions, where the decrease in viscosity upon return from high shear rates is thought to be a consequence of breaking down small floccu-

lates arising from the very weak van der Waals interactions. The presence of very weak van der Waals interactions is suspected because of the slight visual turbidity of the suspensions. However, these interactions are much smaller in magnitude than the electrostatic interactions of the unneutralized dispersion. If the dispersions are allowed to equilibrate after shearing, they are observed to recover to their pre-sheared viscosity and give very reproducible flow behavior. There is no evidence of any shear-induced aggregation for either dispersion, indicating they are inherently stable. More extensive rheological studies of these and similar dispersions with varying particle size and concentration can be found in Refs. 27 and 28.

Figure 2 also demonstrates the shear thickening in both dispersions is reversible, with hysteresis evident only at low applied stresses and at the highest particle concentrations for the charge-neutralized dispersions. However, observe that the shear thickening transition for the charge-neutralized dispersions are shifted to lower stresses as compared to the unneutralized dispersions. The critical shear stresses marking the onset of shear thickening are lower for the neutralized dispersions ($\tau_c \approx 170$ Pa) than for the charged dispersions ($\tau_c \approx 750$ Pa). This result has been shown to be quantitatively predicted from consideration of the incipient formation of hydroclusters.[27,28] In the hydrocluster mechanism for shear thickening, the formation of hydroclusters is predicted to occur when the compressive hydrodynamic forces dominate over the stabilizing repulsive forces. For the unneutralized dispersions the magnitude of the electrostatic repulsive force acting between two particles at these concentrations is calculated to be approximately $7\ k_BT/a$, whereas the Brownian force between the neutralized dispersions is only about half of that ($|F_{\text{Brownian}}| \approx 3\ k_BT/a$) at the same concentration. The reduction in the repulsive force upon charge-neutralization decreases the shear stress required to generate hydroclusters and therefore, shear thickening is observed to occur at lower shear stresses (and shear rates). This result is also in qualitative agreement with the simulation predictions of Melrose and co-workers,[9,14] who demonstrated that the addition of a conservative repulsive force (without any modification of the lubrication stresses) suppresses the onset of shear thickening.

The static SANS spectra of the unneutralized and charge-neutralized dispersions are compared in Fig. 3. The lines are predictions of integral equation theory (Ornstein–Zernike with Rogers–Young closure) using the Yukawa potential for the charge stabilized dispersions and a hard sphere potential for the neutralized dispersion. Satisfactory agreement for the measured and predicted structure factors is observed, validating the particle characterization. Both scattering curves for the neutralized dispersions show much less structure (smaller primary peaks) than the corresponding scattering curves from the unneutralized dispersions. The decrease in the amount of structure in the scattering upon addition of HNO_3 is due the neutralization of the electrostatic interactions that are present in the weakly charged dispersions. Note that the wave vector range is sufficient to incorporate the entire nearest neighbor correlation peak, and thus

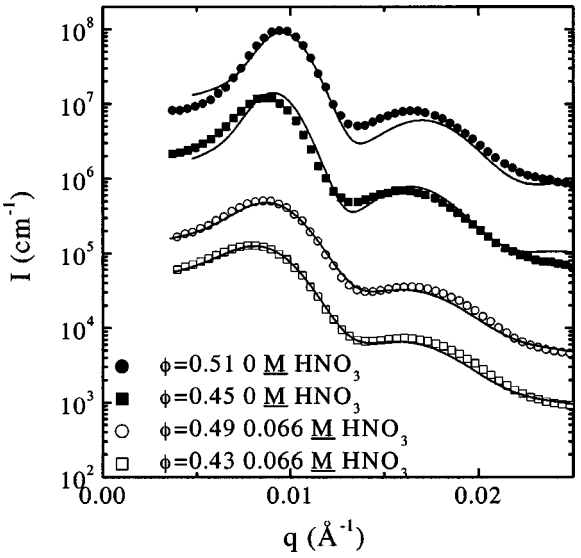

FIG. 3. SANS spectra comparison between the unneutralized (filled symbols) and neutralized (open symbols) dispersions at two particle concentrations ($\phi = 0.5$ and $\phi = 0.43$). The solid lines represent the fits assuming a Yukawa potential and hard sphere potential for the unneutralized and neutralized suspensions, respectively.

we will be able to detect microstructure rearrangements on the scale of nearest neighbor distances.

Figure 4 shows the radial and tangential SANS for the unneutralized dispersion within the shear thinning ($\dot{\gamma} = 100\ \text{s}^{-1}$, top plots) and shear thickening ($\dot{\gamma} = 7000\ \text{s}^{-1}$, bottom plots) regimes. Note that because the shear-induced microstructure distortions are quite small at these high concentrations as compared with the equilibrium scattering, the SANS patterns plotted have a low shear pattern subtracted off, $I(\dot{\gamma}) - I(\dot{\gamma} = 1\ \text{s}^{-1})$. The low shear rate pattern was found, to within measurement accuracy, to be identical to the

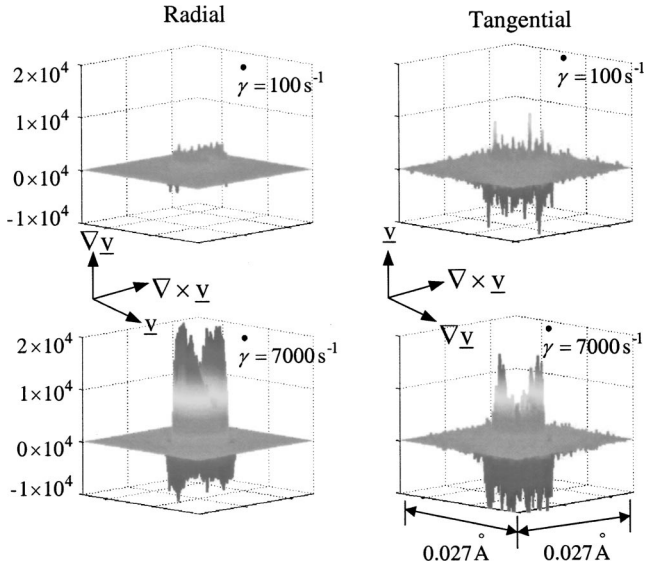

FIG. 4. SANS spectra for the unneutralized dispersions with the spectra at $\dot{\gamma} = 1\ \text{s}^{-1}$ subtracted. The wave vector ranges from 0 to 0.027 Å, and the intensity ranges from -1×10^{-4} to 2×10^{-4} (all axis on same scale). Figures on the left are from a radial configuration and on the right from a tangential configuration.

rest pattern, and has the added benefit of averaging over the sample cell. Note that a signal of zero indicates no distortion by shear, and that negative values are permissible. For both projections, increasing shear rate results in an increase in the difference relative to the rest state. The scattering from the radial geometry shows anisotropy before and during shear thickening, whereas scattering in the tangential geometry displays significant distortion only in the shear thickened state. This two-fold symmetry in the scattering is indicative of microstructure elongation in the flow direction. However, observe there is no evidence of six-fold symmetry, which would occur if the suspension organized into layers of hexagonally close packed particles within the velocity-vorticity plane.[18,21] Moreover, notice that there is an isotropic increase in the scattering intensity near the scattering center, and subsequently a decrease in the scattering intensity at slightly larger wave vectors. This shift in intensity toward smaller scattering angles is indicative of the formation of larger structures, i.e., hydroclusters. We note that these results are in good agreement with the recent SANS studies of Watanabe *et al.*,[13,29] where both tangential and radial SANS projections are presented for a shear-thickening dispersion.

The information contained in Fig. 4 can be conveyed more quantitatively and compactly by integrating the harmonic weighted scattering spectra over the azimuthal angle at a constant wave vector magnitude. The results of the integration for SANS spectra in Fig. 4 are shown in Fig. 5, where the data at $\dot{\gamma}=1\ \mathrm{s}^{-1}$ has been subtracted. Thus, zero indicates no change in the microstructure, while nonzero values indicate the difference to the rest state. The nonweighted, circularly averaged scattering from both the radial and tangential geometries illustrates the shift in the scattering intensity to smaller scattering angles around $q=0.005$ Å. Furthermore, notice that the shift becomes noticeable at shear rates nearly an order of magnitude less ($\dot{\gamma}\sim 100\ \mathrm{s}^{-1}$) than the critical shear rate for shear thickening ($\dot{\gamma}\sim 3000\ \mathrm{s}^{-1}$) and continues to increase until the shear thickening regime, where upon it doesn't change further with increasing shear rate. The two-fold anisotropy is evident in both the radial and tangential scattering from the $\cos(2\phi)$ weighted integration, which also increases systematically with increasing shear rate. No changes in the four-fold symmetry from the $\cos(4\phi)$ harmonic integration is observed to within measurement accuracy. Both the radial and tangential scattering indicate a *very weak* degree of a six-fold symmetry from the $\cos(6\phi)$ harmonic at the highest shear rates. The shifts for this harmonic between the radial and tangential scattering are in opposite directions, which could result from flow structures similar to those seen in nonequilibrium Brownian dynamic simulations.[42,43]

The results of the same analysis procedure applied to the charge-neutralized dispersion are illustrated in Fig. 6 ($I(\dot{\gamma})-I(\dot{\gamma}=0)$). The results for the charge-neutralized dispersion are strikingly different than those for the unneutralized dispersion. Observe from the circularly averaged scattering spectra that no significant changes in the radial scattering occur between the equilibrium and shear thinning states. The radial scattering doesn't change until shear rates in the shear thickening regime ($\dot{\gamma}\geqslant 100\ \mathrm{s}^{-1}$). This contrasts sharply with

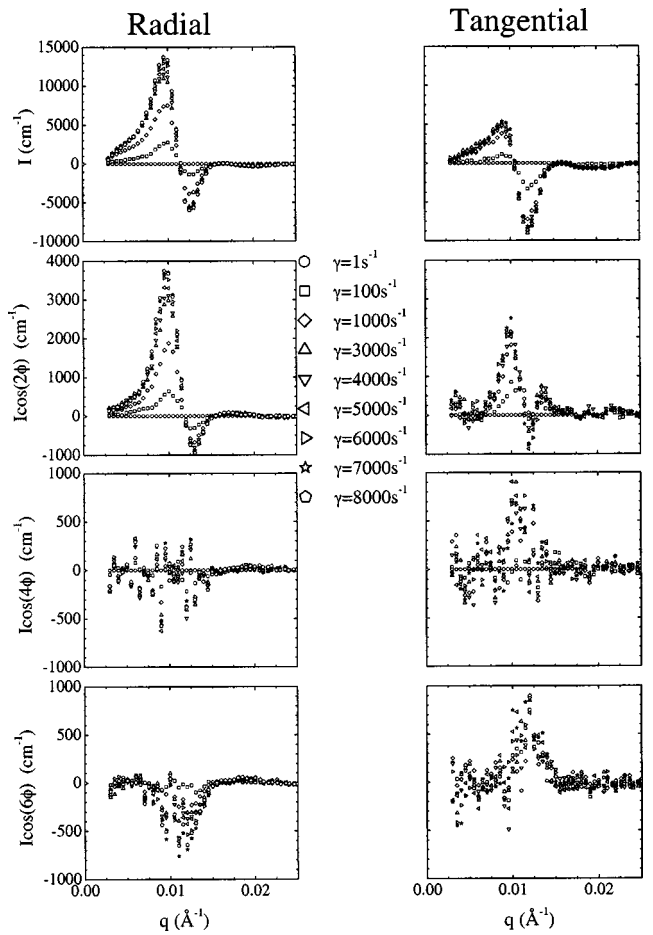

FIG. 5. Harmonic weighted, circularly integrated SANS difference spectra $[I(q,\phi;\dot{\gamma})-I(q,\phi;\dot{\gamma}=1\ \mathrm{s}^{-1})]$ for the unneutralized HS75 dispersion at a volume fraction of 0.5, over a range of shear rates. Data for plots on the left are obtained from radial scattering, and the right obtained from tangential scattering. Note that the scales are expanded for the higher harmonics due to the weaker signal.

the unneutralized dispersions that show systematic shifts throughout shear thinning. Similarly, notice that the charge-neutralized dispersions do not exhibit a detectable two-fold anisotropy in there scattering in the shear thinning state, as indicated by the absence of change in the data from the $\cos(2\phi)$ harmonic integration. However, as in the circularly average data, this harmonic changes abruptly at the point of shear thickening. Finally, notice that there are no noticeable changes in the $\cos(4\phi)$ and $\cos(6\phi)$ harmonics within the scatter of the data. The absence of anisotropy or ordering in *both* the radial and tangential scattering of the neutralized dispersions demonstrates that the shear thickening in this dispersion is not a consequence of an order–disorder transition. However, the shifts in the circularly averaged radial and tangential spectra are in qualitative agreement with the hydrocluster mechanism for shear thickening. Furthermore, the anisotropic growth in the scattering in the shear thickening regime correlates with ellipsoidal hydroclusters lying in the flow-gradient plane and tilted into the flow direction. This is consistent with the simulation results of Brady and co-workers[44] and Melrose and co-workers,[10] where they visualize shear thickening as the jamming of particle clusters aligned along the compressive axis.

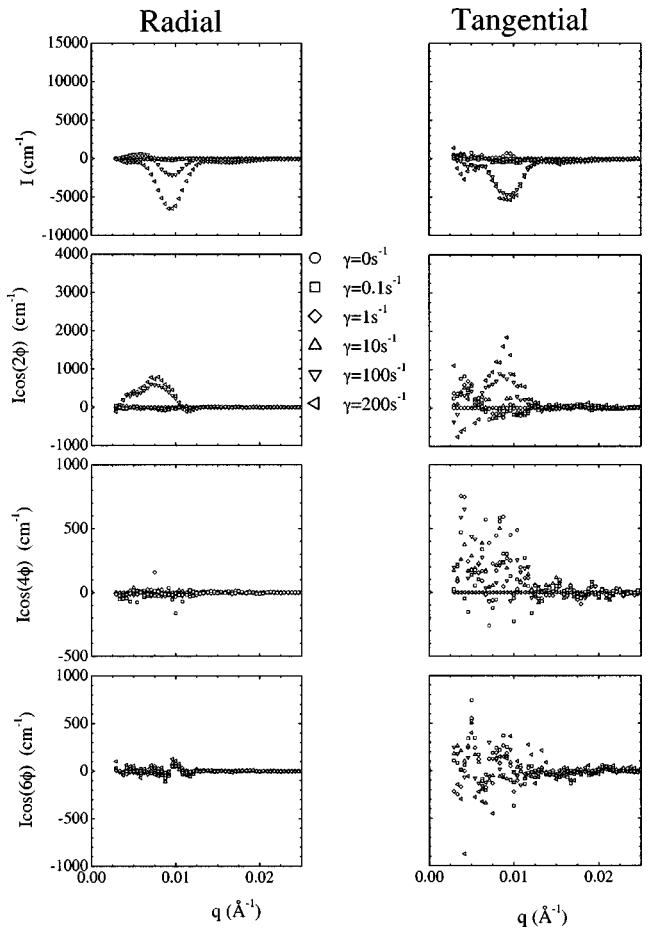

FIG. 6. Harmonic weighted, circularly integrated SANS difference spectra $[I(q,\phi;\dot{\gamma})-I(q,\phi;\dot{\gamma}=1\ \mathrm{s}^{-1})]$ for the neutralized HS75 dispersion at a volume fraction of 0.5, over a range of shear rates. Data for plots on the left are obtained from radial scattering, and the right obtained from tangential scattering. Note that the scales are expanded for the higher harmonics due to the weaker signal.

Figure 7 shows the analyzed SANS scattering for the lesser concentrated unneutralized dispersions ($\phi=0.43$). In this set of plots, the $\cos(4\phi)$ and $\cos(6\phi)$ harmonics are excluded, because there is no observable change in these data with shear rate to within measurement sensitivity. The data are qualitatively similar to the more concentrated dispersion (Fig. 5). Once the shear thickening regime is entered, the scattering changes very little, similar to the more concentrated dispersion.

These harmonic weighted scattering results are used with Eqs. (5)–(7) to reconstruct the true, three-dimensional microstructure under flow. Figures 8–10 illustrate the harmonic functions $B^{+}_{0,0}(q;\dot{\gamma})$, $B^{+}_{2,0}(q;\dot{\gamma})$, and $B^{+}_{2,2}(q;\dot{\gamma})$, respectively [Eqs. (5)–(7)] for the unneutralized HS75 dispersion at $\phi=0.49$ at various shear rates. Notice that the $B^{+}_{0,0}(q;\dot{\gamma})$ harmonic is substantially larger at low shear than either the $B^{+}_{2,0}(q;\dot{\gamma})$ or $B^{+}_{2,2}$ harmonics. The reason for this is that the $B^{+}_{0,0}(q;\dot{\gamma})$ harmonic is a function of the circularly averaged intensity, $W_{0,\mathrm{tangential}}$, whereas the $B^{+}_{2,0}(q;\dot{\gamma})$ and $B^{+}_{2,2}(q;\dot{\gamma})$ harmonics are functions of $\cos(n\phi)$ weighted intensities only. Thus, at asymptotically low deformation rates, where the suspension is isotropic, the $B^{+}_{2,0}(q;\dot{\gamma})$ and $B^{+}_{2,2}(q;\dot{\gamma})$ harmonics vanish. Contrarily, at equilibrium the

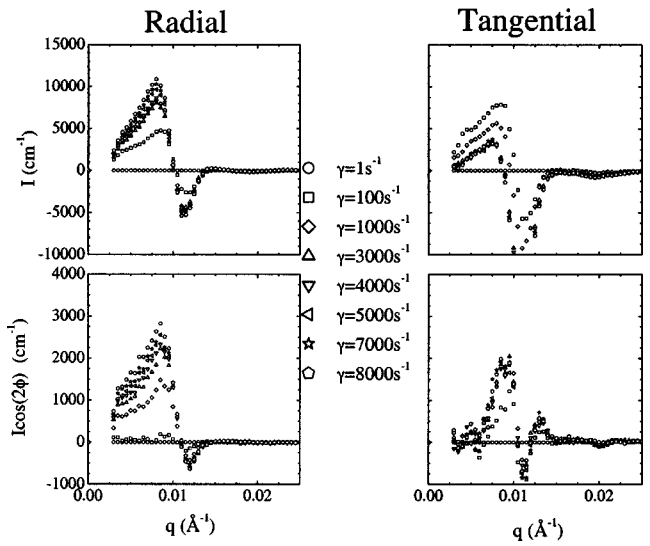

FIG. 7. Harmonic weighted, circularly integrated SANS difference spectra for the unneutralized HS75 dispersion at a volume fraction of 0.43, over a range of shear rates. Data for plots on the left are obtained from radial scattering, and the right obtained from tangential scattering.

$B^{+}_{0,0}(q;\dot{\gamma})$ harmonic is nonzero and represents the equilibrium hydrodynamic contribution to the stress tensor.

The integrals of the harmonics with respect to the wave vector, as suggested by Eqs. (3) and (9), correlate the hydrodynamic component of the shear stress and the thermodynamic component of the normal stress to suspension microstructure, respectively. Figures 11–13 illustrate the change in the hydrodynamic shear stress and thermodynamic normal stresses with increasing shear rate. Note that in calculating the integrals, the integration is stopped at the primary peak in the structure factor in order to minimize the effects of the scatter in the data at higher q (range: $0.0044<q<0.0083$). This is a reasonable approximation, since the hydrodynamic functions that weight the harmonics in the exact integral

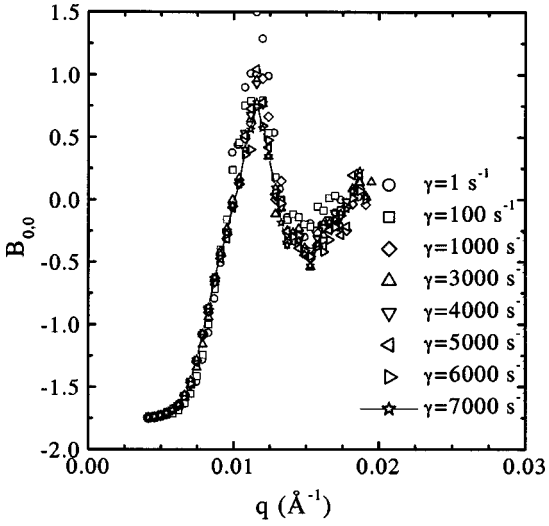

FIG. 8. $B_{0,0}$ harmonic calculated according to Eq. (5) using the SANS spectra from the unneutralized HS75 dispersions at $\phi=0.49$. The line through the data corresponding to the highest shear rate is included to guide the eye.

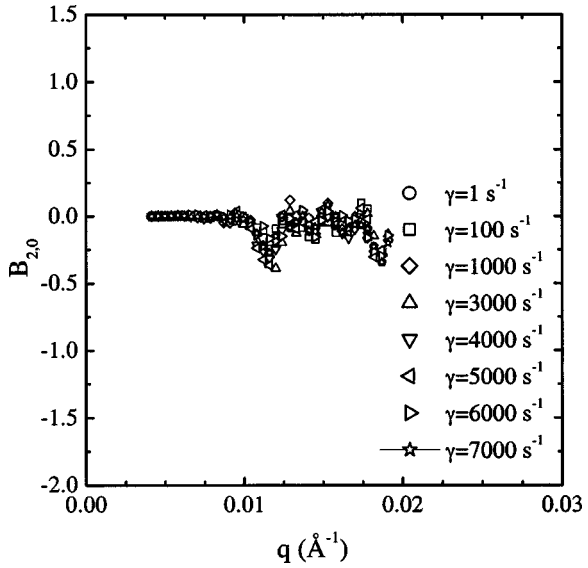

FIG. 9. $B_{2,0}$ harmonic calculated according to Eq. (6) using the SANS spectra from the unneutralized HS75 dispersions at $\phi=0.49$. The line through the data corresponding to the highest shear rate is included to guide the eye.

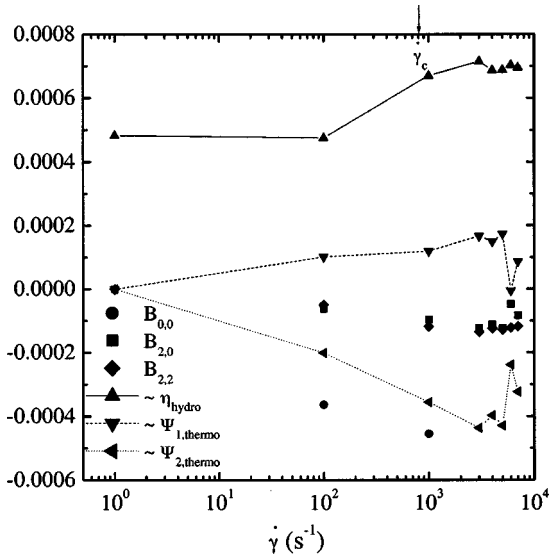

FIG. 11. Several of the harmonics [Eqs. (5)–(7)] and the correlated hydrodynamic stress [Eq. (4) using the SANS spectra from the unneutralized HS75 dispersions at $\phi=0.49$]. The lines are included to guide the eye.

$[\alpha(q),\ \beta(q),\ \xi_0(q)$, and $\xi_2(q)$ in Eq. (3)] decay nearly to zero by $qa\sim 2$. The figures all demonstrate that the hydrodynamic stress increases in magnitude near the shear thickening transition. Furthermore, notice that the change in the hydrodynamic stress for the unneutralized dispersion at $\phi=0.43$ is substantially greater than either of the more concentrated dispersions. This is mainly due to the larger change in the $B^{+}_{0,0}(q;\dot{\gamma})$ harmonic for the less concentrated dispersion, which may be a consequence of increased compressibility. As the dispersion concentration increases there is less volume for the isotropic spatial distribution of the particles to change, and therefore less change in the circularly average scattering spectra. This observation is qualitatively consistent with the ''hydrocluster'' microstructure at shear thickening, where the hydrocluster has a slightly greater local particle density than the unperturbed microstructure.

Figures 11–13 also illustrate the change in the thermodynamic component of the normal stress differences. Each suspension exhibits the same qualitative trends, in which the magnitude of both the first and second normal stress difference increase with increasing shear rate. The increase in the first normal stress difference with increasing shear rate is consistent with hydrocluster formations that align along the compression axis (135° from the flow direction). Furthermore, this result is in qualitative agreement with the Stokesian dynamic simulations by Brady and co-workers.[40] Notice

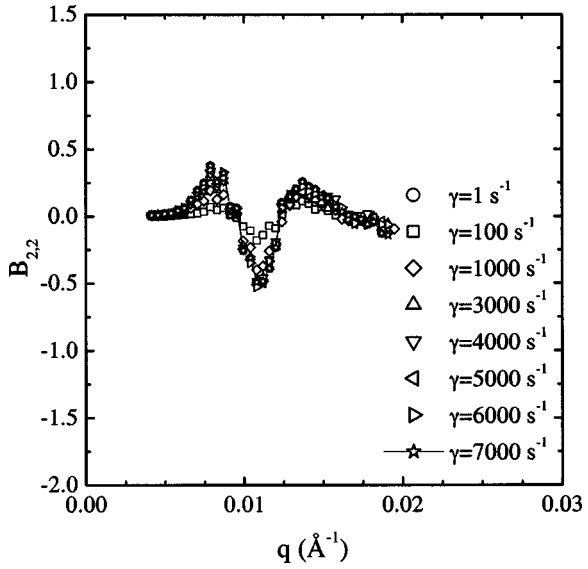

FIG. 10. $B_{2,2}$ harmonic calculated according to Eq. (5) using the SANS spectra from the unneutralized HS75 dispersions at $\phi=0.49$. The line through the data corresponding to the highest shear rate is included to guide the eye.

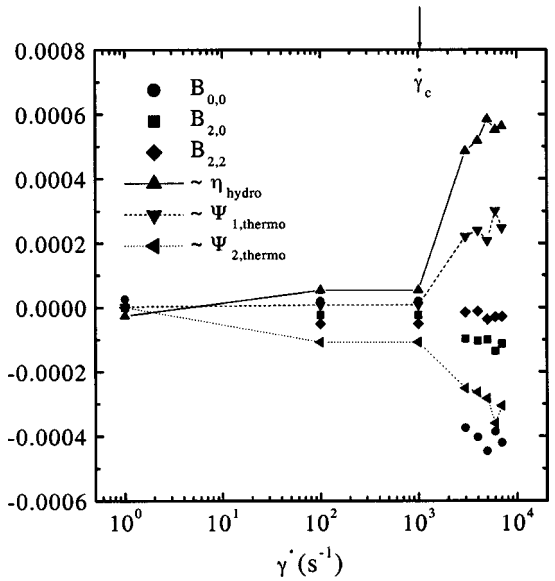

FIG. 12. Several of the harmonics [Eqs. (5)–(7)] and the correlated hydrodynamic stress [Eq. (4) using the SANS spectra from the unneutralized HS75 dispersions at $\phi=0.43$]. The lines are included to guide the eye.

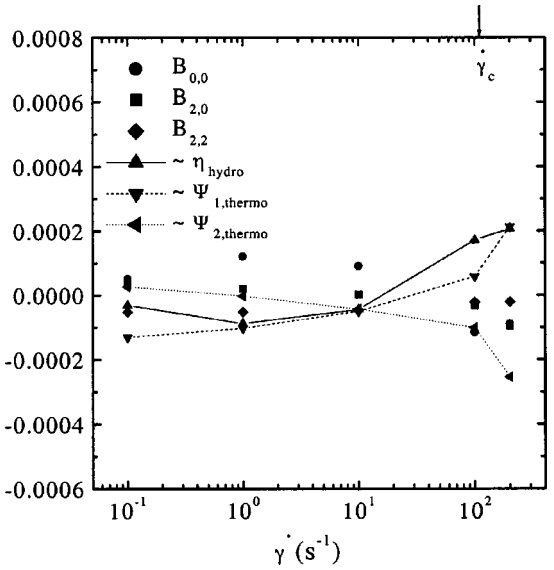

FIG. 13. Several of the harmonics [Eqs. (5)–(7)] and the correlated hydrodynamic stress [Eq. (4) using the SANS spectra from the neutralized HS75 dispersions at $\phi=0.50$]. The lines are included to guide the eye.

that the second normal stress difference (interparticle and Brownian components) is greater in magnitude than the first, until the shear thickening transition, for both potentials. The signs are correct, but the relative order is not in qualitative agreement with theoretical predictions for dilute suspensions.[40,41]

Finally, the Stress-SANS coefficient can be obtained for the charge-stabilized (unneutralized) dispersion by plotting the calculated shear stress against the measured shear stress. Figure 14 shows excellent correlation between the hydrodynamic stress determined from the Rheo-SANS method [i.e., Eq. (4), which has been multiplied by 10^{-2} as an estimate of the magnitude of the hydrodynamic interactions[36]], and the measured shear stress. Note that at low shear stresses, the measured stress is greater than the hydrodynamic component, as there are still substantial contributions from the direct, interparticle interactions. At higher shear stresses and in the shear thickening regime, the measured stress is approximately equal to 1.3 ± 0.1 times the calculated value (the fit line regressed to the data obtained in the shear thickening regime), which provides additional confidence in the analysis. As noted previously, data at very high shear stresses deep into the shear thickening regime is suspect due to significant slip, and is not included here. The deviations in the Stress-SANS relation are consistent with the microstructure saturation due to slip. Although not shown here, the hard sphere dispersion yields qualitatively similar results, but the lower stresses and correspondingly lesser microstructure deformation limits the amount of data available for comparison.

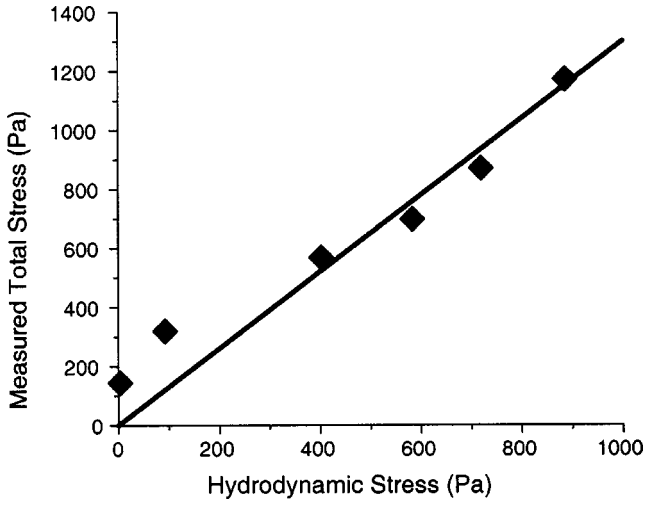

FIG. 14. Stress-SANS plot for charge-stabilized dispersions $\phi=0.49$. The hydrodynamic stress is calculated according to Eq. (4) multiplied by the expected order of magnitude of the coefficient (10^{-2}). The line indicates a Stress-SANS coefficient of 1.3.

IV. DISCUSSION

Neutralization of the surface charge on the weakly electrostatic stabilized dispersions through the addition of 0.066 $\underline{M}$ HNO_3 dramatically lowers the low-shear suspension rheology. The critical stress for shear thickening is also observed to decrease by nearly an order of magnitude upon charge-neutralization. The decrease in the low shear viscosity is attributed to a decrease in the effective volume fraction in the suspension, due to the removal of the electrostatic interactions.[27] The decrease in the critical shear stress for shear thickening upon charge-neutralization is rationalized by a balance between the compressive hydrodynamic forces and the repulsive stabilizing forces.[28] As the electrostatic interactions are removed by charge-neutralization, the magnitude of the repulsive force decreases relative to the Brownian force. This reduction in repulsive force lowers the hydrodynamic force necessary to induce hydroclusters, and hence, lowers the critical stress for shear thickening.

Charge-neutralization also has a profound impact on the equilibrium and shear induced microstructures. At equilibrium, the SANS spectra for the unneutralized dispersions are reasonably predicted by a solution of the Ornstein–Zernike equation for a Yukawa potential to calculate the structure factor, where all the potential parameters are determined from independent measurement.[33] The charge-neutralized dispersions yield SANS spectra that are well predicted with a hard sphere model.[28]

At low shear rates there is a marked difference between dispersions in the anisotropy evident in the SANS spectra. Most noticeably, the charge stabilized dispersions exhibit greater shear-induced microstructure distortion than the charge-neutralized dispersions. This has been predicted from numerical solutions of the Smoluchowski equation by Bergenholtz *et al.*[41] In the absence of interparticle interactions, the microstructure must reflect the for-aft symmetry of low Reynolds number hydrodynamics.[40] However, the added presence of strong electrostatic repulsion leads to the development of strong anisotropy in the microstructure, qualitatively similar to that observed here.

This evolution in microstructure parallels the magnitude of change in the shear rheology, but these microstructural changes at low shear rate are not directly related to the dominant contribution to the shear viscosity (i.e., that from interparticle interactions). Because the SANS patterns explored

here do not probe the $B^+_{2,1}$ component of the deformation, and this deformation is the dominant deformation at low shear and is primarily responsible for the low shear viscosity (see Refs. 36 and 45), the observed flow-induced microstructure anisotropy is primarily representative of the component of the normal stress differences due to interparticle interactions.

At higher shear rates, in the shear thickening regime, the SANS spectra for both the charge-neutralized and unneutralized dispersions behave similarly in that the scattering intensity shifts to lower scattering angles. Note further that in the transition from the shear thinning to shear thickening the anisotropy of the unneutralized dispersion continues to increase, and similarly the charge-neutralized dispersion begins to exhibit an anisotropy with two-fold symmetry. However, neither of the dispersions exhibit a melting of a six-fold scattering symmetry, which is a characteristic of the destabilization of hexagonal-close packed layers. As there is no evidence for order in any of the dispersions at rest or under shear, the SANS results shown here demonstrate that an ODT is not necessary for shear thickening. As noted, these results are in complete agreement with other, recent SANS studies of dispersions under flow.[13,29]

As the shear rate is further increased within the shear thickened state, there is no apparent change in the microstructure. This may be a consequence of wall slip in the shear thickening regime. An earlier investigation[27] shows that increasing the shear stress beyond the critical stress for shear thickening leads to an increasing slip velocity, in which the true shear rate does not change. Consequently, saturation in the patterns at high shear rates is consistent with the presence of extreme wall slip.

The harmonic coefficients of the scattering presented here (i.e., $B^+_{l,m}$) have a one-to-one correspondence to the real space structure and hence, it is possible to interpret the scattering results represented in this form directly in terms of real space structure. The real space expansion written in the radial (on-axis) laboratory frame is:[36]

$$h(r)=\frac{1}{\sqrt{\pi}}P_{o,o}+\sqrt{\frac{5}{4\pi}}P_{2,0}(3\hat{z}^2-1)+\sqrt{\frac{15}{2\pi}}P_{2,1}\hat{z}\hat{x}+\sqrt{\frac{15}{8\pi}}P_{2,2}(\hat{x}^2-\hat{y}^2)+\ldots, \tag{10}$$

where the coefficients $P_{l,m}$ are functions of the particle separation distance r and shear rate. These coefficients are Henkel transforms of the $B^+_{l,m}$ scattering coefficients. Although it is not possible to give a general result for the sign of all the coefficients, for the data presented here the zero order transform will have the same sign, whereas the second order transform ($l=2$) will have the opposite sign.

Examining Figs. 8–10 with these transformation rules suggest that the charge stabilized dispersion has a real space structure with the following features. The large increase in $B^+_{0,0}$ corresponds to an increase in the density of nearest neighbors under flow. The primarily negative result for $B^+_{2,0}$ suggests increases in particle density in the flow gradient direction. This is what is predicted by simulation and calculation.[40,41] The function $B^+_{2,2}$ exhibits a more complex structure, but is dominated at high shear rates in the shear thickening regime by the negative peak. This would correspond to an increase in neighbor density along the flow direction relative to the vorticity direction.

The theoretical calculations of Bergenholtz, Brady, and Vicic[41] comparing hard sphere dispersions with hard sphere dispersions with an extended excluded hard sphere potential can be qualitatively compared with the experimental evidence for hard sphere and electrostatically stabilized suspensions presented here. The rheological results for the suppression of the onset of shear thickening with increasing excluded volume corresponds with the shift of the onset of shear thickening to higher applied shear rates and stresses with electrostatic stabilization. As significantly, the greater microstructure deformation and higher degree of anisotropy for the charge-stabilized dispersion is qualitatively in agreement with the predictions for dispersions with excluded volume interactions beyond the hard sphere repulsion.

Correlation of the suspension microstructure to the hydrodynamic component of the shear stress indicates that the magnitude of the hydrodynamic shear stress monotonically increases with increasing shear rate. Furthermore, the hydrodynamic stress is observed to rapidly increase near the shear thickening transition. This is consistent with the increase in hydrodynamic stresses due to lubrication forces within hydroclusters. Similar correlations between the suspension microstructure to the thermodynamic component of the normal stress differences demonstrates that the first normal stress difference increases during shear thickening. This also supports the hydrocluster mechanism for shear thickening, as the hydroclusters are aligned along the compression axis.

V. CONCLUSION

A new method of Rheo-SANS has been demonstrated and employed to validate that reversible shear thickening in dense, colloidal suspensions is a consequence of hydrodynamic interactions. Both electrostatically stabilized and charge-neutralized, near hard sphere dispersions were examined. The charge-stabilized dispersions exhibited much higher low shear rate viscosities and commensurately larger microstructure deformations than the charge-neutralized dispersions, in qualitative agreement with recent theoretical predictions and simulations. The neutralized dispersion begins to exhibit significant microstructural anisotropy and flow-induced microstructure near the shear-thickening transition. From analysis of both the tangential and radial scattering spectra, the three-dimensional microstructure of the charge-stabilized dispersion is observed to develop a strong flow-induced anisotropy, but without any long-range order either prior to or after shear thickening, i.e., there is no order–disorder transition accompanying the observed shear thickening. For both types of dispersions, the SANS intensity intensifies at lower scattering angles as the sample shear thickens, in qualitative agreement with simulations and theory that predict shear thickening as a consequence of shear-induced ''clustering'' of the particles. Quantitative analysis of the shear-induced microstructure demonstrates

that the hydrodynamic component of the shear stress is responsible for the observed increase in the measured stress. A stress-SANS rule is observed through the shear-thickening transition and the stress-SANS coefficient is found to be in quantitative agreement with prediction. These observations support the theoretical results and simulation predictions that reversible shear thickening is a consequence of increased short-range hydrodynamic interactions that manifests as the formation of hydroclusters in the flow field.

ACKNOWLEDGMENTS

The authors thank Professor J. Brady for making useful discussions and for providing preprints of the theoretical calculations. This work was supported by the National Science Foundation (CTS-9523268) and the International Fine Particle Research Institute. The SANS measurements were performed at the National Institute of Standards and Technology under agreement NSF DMR-912244.

APPENDIX: RECONSTRUCTION OF EXPANSION FUNCTIONS

The goal of the method is to reconstruct the expansion functions of the structure factor $B^+_{l,m}$ from two dimensional SANS spectra. Two geometries are considered, but the approach is general and can be applied to any geometry. However, note that for the geometries considered here, the equations simplify because of the assumption of *small angles*, i.e., the detector is considered to be ''flat'' and truly two dimensional.

The transformation from the 3-D scattering function $S(\mathbf{q})$ to the detector pattern in 2-D is accomplished via the spherical harmonic expansion. The values of the scattering vector $\mathbf{q}$ are then calculated for the plane of the detector. A simplification can generally made for the case of SANS, as for small angles, $q_z \approx 0$, where $\hat{z}$ is the propagation direction of the neutron beam.

In the article by Wagner and Ackerson,[36] the geometry corresponds to scattering down the gradient direction of the flow (i.e., *z*-direction), with the flow along the *x*-direction. This was chosen for calculational convenience. Standard, on axis or radial scattering has the incident wave vector aligned with the velocity gradient axis. The flow direction is ''horizontal'' on the detector, while the vorticity direction is ''vertical'' on the screen. First, in this geometry and in the assumption of small angle, the value of $q_z \approx 0$. Consequently, there is no need to consider that the light passes through the cell twice, As the detector actually averages over both $+\nabla \mathbf{v}$ and $-\nabla \mathbf{v}$. However, the expansion is symmetric in this variable for all terms that are not multiplied by q_z and the SANS pattern is symmetric in the $\hat{x}$ or horizontal direction.

In this geometry, the scattering function has the Cartesian expansion with the first few terms:

$$\hat{h}(\mathbf{q}) = \frac{1}{\sqrt{\pi}} B^+_{0,0} + B^+_{2,0}\sqrt{\frac{5}{4\pi}}(-1) + B^+_{2,2}\sqrt{\frac{15}{8\pi}}\frac{(q_x^2 - q_y^2)}{q^2} + \dots . \tag{A1}$$

The weighted integrals over the detector are now evaluated, with the index (radial) denoting the scattering orientation, and (n) the weighting. The angle ϕ is defined in terms of the horizontal (i.e., flow, $\hat{x}$) direction. Note that the polar angle θ is zero, as per the small angle assumption,

$$W_{n,\text{radial}} = \frac{1}{2\pi}\int_0^{2\pi} \cos(n\phi)\frac{S(\mathbf{q})}{S_{\text{eq}}(\mathbf{q})}\,d\phi = \frac{1}{2\pi}\int_0^{2\pi} \cos(n\phi)\frac{h(\mathbf{q})+1}{S_{\text{eq}}(q)}\,d\phi. \tag{A2}$$

Integration leads to

$$W_{0,\text{radial}} = \frac{1}{S_{\text{eq}}}\left(1 + B^+_{0,0}\sqrt{\frac{1}{\pi}} - B^+_{2,0}\sqrt{\frac{5}{4\pi}} + \dots\right),$$

$$W_{2,\text{radial}} = \frac{1}{S_{\text{eq}}}\left(\frac{1}{2}B^+_{2,2}\sqrt{\frac{15}{8\pi}} + \dots\right),$$

$$W_{4,\text{radial}} = 0 + \dots, \tag{A3}$$

where the higher order terms have been neglected.

These relations can be inverted, with the help of the following, tangential scattering results, to solve for the coefficients of the spherical harmonic expansion.

Idealized, off axis or tangential scattering has the incident wavevector aligned with the velocity axis. The flow gradient direction is ''horizontal'' on the detector, while the vorticity direction is ''vertical'' on the screen. Note that the vorticity direction (vertical) is common to both on and off axis scattering. In this geometry and for small angles ($q_z = 0$) the scattering function has the Cartesian expansion:

$$\hat{h}(\mathbf{k}) = \frac{1}{\sqrt{\pi}}B^+_{0,0} + B^+_{2,0}\sqrt{\frac{5}{4\pi}}\left(3\frac{q_x^2}{q^2} - 1\right) + B^+_{2,2}\sqrt{\frac{15}{8\pi}}\frac{(-q_y^2)}{k^2} + \dots . \tag{A4}$$

The weighted integrals over the detector are now evaluated in this rotated frame of the detector, with the index (tangential) denoting the scattering orientation, and (n) the weighting as per Eq. (A2). The angle ϕ is defined in terms of the horizontal (i.e., flow, $\hat{x}$ direction). Note that the polar angle θ is zero, as per the small angle assumption,

$$W_{n,\text{tangential}} = \frac{1}{2\pi}\int_0^{2\pi} \cos(n\phi)\frac{S(\mathbf{q})}{S_{\text{eq}}(q)}\,d\phi = \frac{1}{2\pi}\int_0^{2\pi} \cos(n\phi)\frac{h(\mathbf{q})+1}{S_{\text{eq}}(q)}\,d\phi. \tag{A5}$$

The following results are obtained for the weighted detector integrals:

$$W_{0,\text{tangential}} = \frac{1}{S_{\text{eq}}}\left(1 + B^+_{0,0}\sqrt{\frac{1}{\pi}} + \frac{1}{2}B^+_{2,0}\sqrt{\frac{5}{4\pi}} - \frac{1}{2}B^+_{2,2}\sqrt{\frac{15}{8\pi}} + \dots\right),$$

$$W_{2,\text{tangential}} = \frac{1}{S_{\text{eq}}}\left(\frac{3}{4}B^{+}_{2,0}\sqrt{\frac{5}{4\pi}} + \frac{1}{4}B^{+}_{2,2}\sqrt{\frac{15}{8\pi}} + \ldots\right),$$

$$W_{4,\text{tangential}} = 0 + \ldots, \tag{A6}$$

where the higher order terms have been neglected.

These relations are inverted to solve for the coefficients of the spherical harmonic expansion,

$$B^{+}_{0,0}\sqrt{\frac{1}{\pi}} = \frac{1}{3}S_{\text{eq}}(2W_{0,\text{radial}} + W_{0,\text{tangential}} + 2W_{2,\text{tangential}}) - 1$$

$$= \frac{1}{3}S_{\text{eq}}(W_{0,\text{radial}} + 2W_{0,\text{tangential}} + 2W_{2,\text{radial}}) - 1,$$

$$B^{+}_{2,0}\sqrt{\frac{5}{4\pi}} = \frac{1}{2}S_{\text{eq}}\left(\frac{-2}{3}W_{0,\text{radial}} + \frac{2}{3}W_{0,\text{tangential}} + \frac{4}{3}W_{2,\text{tangential}}\right)$$

$$= \frac{4}{3}S_{\text{eq}}\left(W_{2,\text{tangential}} - \frac{1}{2}W_{2,\text{radial}}\right),$$

$$B^{+}_{2,2}\sqrt{\frac{15}{8\pi}} = 2S_{\text{eq}}W_{2,\text{radial}}. \tag{A7}$$

Keeping only the spherical and second order tensorial deformations of the microstructure leads to a set of relations that permit reconstruction of the 3-D spherical harmonic expansion coefficients from weighted integrations over two orthogonal scattering patters (radial and tangential). Note, however, that for these geometries the dominant linear deformation term $B^{+}_{2,1}$ *is not accessible by small angle scattering*. Previous work[34] has shown that for wide angle light scattering, this term is accessible. The terms treated here are important for the interparticle potential contribution to the normal stresses, as well as the hydrodynamic stress contribution to the viscosity. The method can be extended to higher order terms in the expansion, as well as higher order integrals. Note that the higher order detector integrals of fourth order do not contain information about the second order tensorial terms, but rather, only reflect higher order terms in the expansion. Thus, the fourth and sixth (which is of special interest for the detection of hexagonal crystal symmetry) order detector integrals provide information about the importance of higher order terms in the spherical harmonic expansion.

[1] R. L. Hoffmann, Trans. Soc. Rheol. **16**, 155 (1972).
[2] R. L. Hoffmann, J. Colloid Interface Sci. **46**, 491 (1972).
[3] R. L. Hoffmann, Mater. Res. Bull. **16**, 32 (1991).
[4] W. H. Boersma, J. Laven, and H. N. Stein, J. Colloid Interface Sci. **149**, 10 (1992).
[5] H. M. Laun, R. Bung, S. Hess, W. Loose, O. Hess, K. Hahn, E. Hadicke, R. Hingmann, F. Schmidt, and P. Lindner, J. Rheol. **36**, 743 (1992).
[6] J. W. Bender and N. J. Wagner, J. Colloid Interface Sci. **172**, 171 (1995).
[7] J. W. Bender and N. J. Wagner, J. Rheol. **40**, 899 (1996).
[8] T. N. Phung and J. F. Brady, J. Fluid Mech. **313**, 181 (1996).
[9] J. R. Melrose, J. H. van Vliet, and R. C. Ball, Phys. Rev. Lett. **77**, 4660 (1996).
[10] R. S. Farr, J. R. Melrose, and R. C. Ball, Phys. Rev. E **55**, 7203 (1997).
[11] J. F. Brady and G. Bossis, Annu. Rev. Fluid Mech. **20**, 111 (1988).
[12] R. L. Hoffmann, J. Rheol. **42**, 111 (1998).
[13] M. C. Newstein, H. Wang, N. P. Balsara, A. A. Lefebvre, Y. Shnidman, H. Watanabe, K. Osaki, T. Shikata, H. Niwa, and Y. Morishima, J. Chem. Phys. **111**, 4827 (1999).
[14] A. A. Catherall, J. R. Melrose, and R. C. Ball, J. Rheol. **44**, 1 (2000).
[15] P. D'Haene, J. Mewis, and G. G. Fuller, J. Colloid Interface Sci. **156**, 350 (1993).
[16] B. Kaffashi, V. T. OBrien, M. E. Mackay, and S. M. Underwood, J. Colloid Interface Sci. **181**, 22 (1997).
[17] V. T. OBrien and M. E. Mackay, Langmuir **16**, 7931 (2000).
[18] M. K. Chow and C. F. Zukoski, J. Rheol. **39**, 33 (1995).
[19] M. K. Chow and C. F. Zukoski, J. Rheol. **39**, 15 (1995).
[20] H. M. Laun, R. Bung, and F. Schmidt, J. Rheol. **35**, 999 (1991).
[21] R. J. Butera, M. S. Wolfe, J. Bender, and N. J. Wagner, Phys. Rev. Lett. **77**, 2117 (1996).
[22] G. Bossis and J. F. Brady, J. Chem. Phys. **91**, 1866 (1989).
[23] L. E. Silbert, J. R. Melrose, and R. C. Ball, Mol. Phys. **96**, 1667 (1999).
[24] J. F. Brady, Curr. Opin. Colloid Interface Sci. **1**, 472 (1996).
[25] J. R. Melrose and R. C. Ball, *XIIIth International Congress of Rheology*, 2-421 (2000).
[26] W. J. Frith, P. d'Haene, R. Buscall, and J. Mewis, J. Rheol. **40**, 531 (1996).
[27] B. J. Maranzano and N. J. Wagner, J. Chem. Phys. **114**, 10514 (2001).
[28] B. J. Maranzano and N. J. Wagner, J. Rheol. **45**, 1205 (2001).
[29] H. Watanabe, M.-L. Yau, K. Osaki, T. Shikata, H. Niwa, Y. Morishima, N. P. Balsara, and H. Wang, Rheol. Acta **37**, 1 (1998).
[30] A. P. Philipse and A. Vrij, J. Colloid Interface Sci. **128**, 121 (1988).
[31] A. van Blaaderen, J. van Geest, and A. Vrij, J. Colloid Interface Sci. **154**, 481 (1992).
[32] A. van Blaaderen and A. Vrij, J. Colloid Interface Sci. **156**, 1 (1993).
[33] B. J. Maranzano, N. J. Wagner, G. Fritz, and O. Glatter, Langmuir **16**, 10556 (2000).
[34] N. J. Wagner and W. B. Russel, Phys. Fluids A **2**, 491 (1990).
[35] R. A. Lionberger and W. B. Russel, J. Rheol. **41**, 399 (1997).
[36] N. J. Wagner and B. J. Ackerson, J. Chem. Phys. **97**, 1473 (1992).
[37] J. M. Amante, "*Investigation of Shear Thickening in Charge Stabilized Colloidal Dispersion*," Masters thesis, University of Delaware, 1998.
[38] N. J. Wagner, R. Krause, A. R. Rennie, B. D'Aguanno, and J. Goodwin, J. Chem. Phys. **95**, 494 (1991).
[39] J. F. Brady, J. Chem. Phys. **99**, 567 (1993).
[40] J. F. Brady and J. F. Morris, J. Fluid Mech. **348**, 103 (1997).
[41] J. Bergenholtz, J. F. Brady, and M. Vicic, J. Fluid Mech. **456**, 239 (2002).
[42] S. R. Rastogi, "*Nonequilibrium Brownian Dynamics of Colloidal Suspensions*," Ph.D. thesis, University of Delaware, 1995.
[43] S. R. Rastogi, N. J. Wagner, and S. R. Lustig, J. Chem. Phys. **104**, 9249 (1996).
[44] T. N. Phung and J. F. Brady, "Microstructured fluids: Structure, diffusion and rheology of colloidal dispersions," *Slow Dynamics in Condensed Matter*, p. 256.
[45] J. C. Vanderwerff, B. J. Ackerson, R. P. May, and C. G. Dekruif, Physica A **165**, 375 (1990).